Journal of Mechanics, 2010, Volume 26, Number 4, Pages 553-561 DOI: 10.1017/S1727719100004755

Micromechanical modelling of superelasticity in polycrystalline Ni-Ti with non-constant Young's modulus

Andrej Pukšič*, Janez Kunavar, Miha Brojan, and Franc Kosel

Faculty of Mechanical Engineering, University of Ljubljana, Aškerčeva 6, 1000 Ljubljana, Slovenia

Key words Shape memory alloys, micromechanical modelling, return mapping, material texture, finite element method.

We demonstrate a computational model for the application of the micromechanical approach to modeling of superelasticity in shape memory alloys. The model is based on finite element method, where each finite element represents a single crystal grain in the polycrystalline structure. The constitutive equations are integrated at each Gauss point by a return mapping algorithm. In this manner good stability and convergence of the model is achieved. Material properties for Ni-Ti alloy (50.8 at.% Ni) obtained from literature and from our own experiments were applied to the model and a sample calculation of a 3D model subjected to uniaxial loading was performed. The results were compared to experimental results obtained from tensile and compressive tests on a universal testing machine. In general the presented model predicts well the level of the superelastic stress plateau and maximum transformation strain in tension. Predictions in compression do not agree well with the experimental findings but the overall characteristics of the tension-compression asymmetry are predicted correctly.

1 Introduction

Shape memory alloys (SMA) are considered smart materials due to their capability to recover their original shape after being subjected to a certain thermomechanical loading. The term superelasticity (also pseudoelasticity) refers to the capability of shape memory alloys to recover their original shape upon unloading after sustaining considerable deformation (of the order of 8 %) under an applied mechanical load. The reason for shape recovery lies in the thermoelastic martensitic transformation during which the crystal structure of a material changes. To exhibit superelastic properties a material must initially be in a high-temperature phase called austenite or parent phase. Under mechanical loading the initially austenitic material undergoes stress-induced martensitic transformation (forward transformation) and austenite is transformed to martensite. The properties of the transformation are such that large strains can be accommodated without producing plastic (unrecoverable) strains. During unloading martensite reverts to the parent phase in its original orientation (reverse transformation), therefore the material regains its original shape. A typical response of a one-dimensional element (e.g. wire) subjected to a uniaxial loading cycle is shown on Fig. 1. At point A the critical stress for the onset of martensitic transformation is reached, which is reflected in the σ-ε diagram as a radical reduction in stiffness. The martensitic transformation progresses at practically the same stress level (depending on the type of material) until the whole material is transformed to martensite (point B). On the σ-ε diagram this is again noted by the radical change in stiffness. During unloading the material begins to transform back to austenite when critical stress for reverse transformation is reached (point C). This stress is lower than the critical stress for the forward transformation as a consequence of energy dissipation during martensite growth and a typical hysteresis loop can be observed.

From an engineering standpoint of view the most interesting characteristics of a superelastic material are the level of the stress plateau of forward and reverse transformation, the maximum recoverable strain and the temperature dependence of the response. Therefore, a good material model should predict well these three characteristics. However, because of the complexity related to the martensitic transformation (dependence on stress, temperature, loading history and microstructure) the constitutive behaviour of SMA is difficult to predict. Nevertheless, a few models were developed that can be used effectively for predicting superelastic response under different loading conditions. For problems of uniaxial tension see for example [1], [2] and [3], bending of superelastic beams has also been widely studied, see for example [4] and [5]. Recently major efforts have been put towards obtaining a more general three-dimensional model, see for example [6-12], as it is expected that further interesting behaviour could be observed under multi-axial loading as reported in [13] and [14]. Interested reader can find a more extensive review of the existing models in a recent review paper by Patoor et al. [15].

* Corresponding author, e-mail: andrej.puksic@fs.uni-lj.si, Phone: +386 1 4771 609

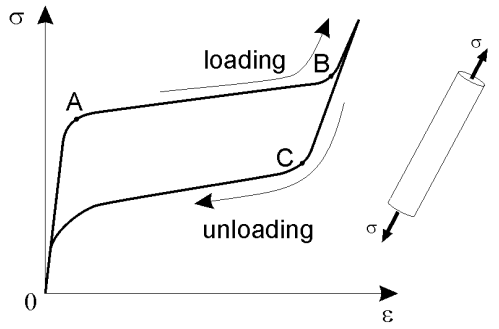

Fig. 1 Typical superelastic response of a one-dimensional SMA element.

Most of the published material models utilize one of the two main approaches to constitutive modelling of SMA: the phenomenological or the micromechanical approach. The former derives the constitutive equations based on macroscopical observations utilizing the methodology known from modelling of plasticity. The main advantage of such approach is that material parameters can usually be identified by classical experiments and that the resulting equations can be solved numerically by well established methods from plasticity modelling. Therefore, such models are suitable for engineering practice. However, since most of the experimental data is obtained from uniaxial tests theese models are difficult to expand to three dimensions. On the other hand, the micromechanical approach is based on studying crystallographic and microstructural properties of martensitic transformation at the crystal grain scale, while macroscopical properties are predicted utilizing multi-scale modelling techniques. Such approach in itself bears no limitations as to the loading conditions (multi-axial or uniaxial) and can be implemented in three dimensions directly. However, the material parameters should be determined on single crystal specimens which are difficult to obtain for some materials. Another disadvantage of modelling macroscopical structures with micromechanical models is the high computational intensity required to simulate large structures. However, with advance of microprocessor technology calculations with multi-scale methods can be performed in reasonable time.

The application of the micromechanical approach to SMAs is justifiable, since the mechanisms of martensitic transformation at the crystal lattice level can be well described applying the ideas of continuum theory of crystalline solids introduced by Ericksen [16-19], see also [20]. The formation of microstructure can be predicted by the phenomenological theory of martensitic transformation originally developed by Bowles and Mackenzie [21, 22] or rather by a more general approach of energy minimization presented by Ball and James [23]. The mentioned theories are proven to describe well the fundamental behaviour of martensitic transformation at the crystal lattice level. However, at the crystal grain level additional complexity related to the interaction of austenite and martensite arises. Therefore, during the derivation of constitutive equations various assumptions can be made that significantly effect the quality of predictions. In this paper we will mainly focus on the effect of the difference in elastic properties of martensite and austenite. This issue is extensively studied by Wang [24] who developed an explicit integration scheme which requires relatively small load steps to converge. Thamburaja [12] also takes account of different elastic properties in his calculations but he does that ad-hoc after the thermodynamical driving force has been derived under assumption of equal elastic properties (see Chapter 2 for details). In this manner some of the computational complexity is avoided but the effect of non-constant elastic properties on superelastic stress plateau is neglected. Effects that are not addressed in the presented model include the effect of irregularities in the microstructure (e.g. dislocations, precipitates) [25], the reorientation and detwinnning of martensite [26] and thermomechanical coupling [27, 28], among others.

If polycrystals are studied, relations between crystal grains should be described. To avoid further physical complexity, we adopt the scheme proposed by Anand [29], where polycrystals are modeled by means of the finite element method (FEM). Such approach also allows the study of effect of material texture, which is the main reason for the tension-compression asymmetry observed in superelastic specimens [12, 30]. Polycrystals can be modeled exactly using modern imaging techniques [31], can be of a random structure resembling a generic polycrystal by using Voronoi diagrams [32] or can be simplified by using finite elements of regular shapes (squares, triangles, cubes etc.). In general, simulations with regular shaped elements provide reasonable results for the macroscopic stress-strain curves [31], which is what will be focused on in this paper. Furthermore, we chose to model each grain with only one finite element. Breaking a crystal grain into more finite elements would result in better insight into local state inside the crystal grain, but that is not of our interest. The presented approach is computationally very intensive therefore efforts to achieve effective algorithmic treatment and reduce computation time are very

important. In our model this is achieved by applying an implicit scheme which enables calculations with larger load steps. Furthermore, strategy for active variants selection is proposed and a sub-stepping algorithm [33] to automatically adjust load steps is utilized.

This paper is organized as follows: for sake of completeness and better understanding of the subject we will first briefly present the fundamentals of deriving the constitutive equations based on micromechanics of SMA. Next, a numerical model based on the finite element method will be presented. Special emphasis will be given to the strategy of active variants selection and to the implementation of non-constant elastic properties. The scope of our work is also to compare the numerical results to the experimental results in order to evaluate quantitatively the performance of the presented model. The comparison will be done on a uniaxial case of loading since good experimental results can be obtained, mainly in the form of a σ-ε diagram as shown on Fig. 1. Examples of calculations on a cube consisting of 343 grains subjected to uniaxial loading will be shown. The experimental section of this paper will also provide detailed information about procedures used to determine material parameters.

2 Constitutive equations

When using the micromechanical approach we distinguish between three scales. Namely, the microscopic scale which is the scale of the microstructure at the crystal lattice level, the mesoscopic scale which is the scale of a crystal grain and the macroscopic scale which is the scale of a polycrystal (Fig. 2).

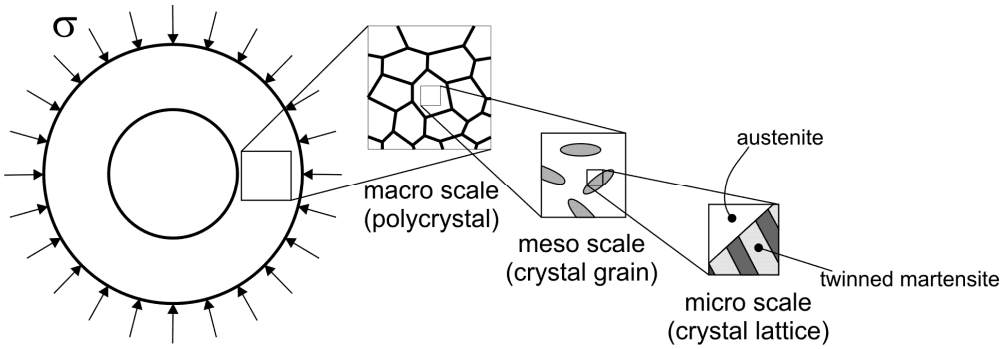

Fig. 2 Different scales utilized in the micromechanical approach.

Since martensitic transformation is diffusionless it can be considered at the microscopic scale as a continuum deformation of the crystal lattice. The deformation is described by a transformation matrix that links the martensitic and the austenitic lattice. The transformation matrix can be calculated if lattice constants of both lattices are known. Due to different symmetries of the lattices there are more than one transformation matrices possible. It is said that different variants, called lattice correspondence variants (CPV), exist. In case of SMAs the austenitic lattice always has higher symmetry, hence different martensitic lattice variants exist. The austenitic lattice of Ni-Ti is cubic, while the martensitic lattice is monoclinic (Fig. 3), therefore there are 12 possible variants (CPV) of martensitic crystal lattice due to loss of symmetry.

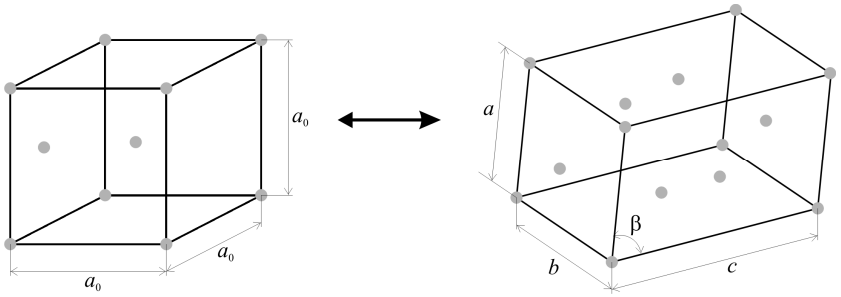

Fig. 3 The austenitic (left) and the martensitic (right) lattice of Ni-Ti alloy.

As a consequence of energy minimization [20] compatible martensitic variants form so called twins (Fig. 4) (two variants form an interface called the twin boundary). It can be shown that in Ni-Ti a single variant of martensite cannot form a coherent interface with austenitic lattice. However, a coherent interface can be formed between a fine mixture of martensitic twins and austenite (Fig. 4). The interface is actually not sharp (it has some finite thickness), but from the mesoscopic point of view it is considered to be a plane and it is called a habit plane. In Ni-Ti there are theoretically 192 possible interfaces between austenite and martensitc twins, but only 24 have been experimentally observed [20]. Therefore it is commonly said that 24 habit plane variants of martensite (HPV) exist. Each of the 24 variants is identified by a vector normal to the habit plane (m_i^r) and a directional vector (b_i^r), where r= 1, ..., 24 denotes the variant*. Both vectors can be calculated from the crystallographic theory of martensitic transformation, given that the lattice parameters of austenite and martensite are known.

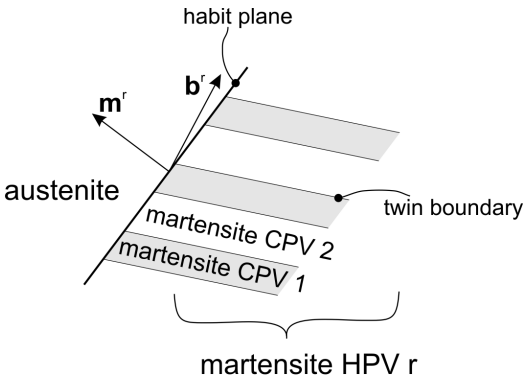

Fig. 4 Twinning in martensite and the definition of habit plane variants.

In a crystal grain the crystal lattice is ideally homogenous so it is reasonable to define a crystal grain to be our representative volume element (RVE). A single crystal grain can be considered a solid body subjected to boundary conditions in form of traction or displacements. The reference configuration of a grain is defined as the configuration when material is fully austenitic and unloaded. The areas of martensite that form when the transformation is in progress can be considered as inclusions (if equal elastic properties of both phases are assumed) or inhomogeneous inclusions (if different elastic properties are assumed) in view of the Eshelby's theory of inclusions [34]. Since martensite is formed in twins we can think of HPVs as the basic »units« of martensite at the mesoscopic level. If micromechanical analysis is to be performed, the intrinsic deformation (eigenstrain) of each martensitic domain must be determined. With normal and directional vector known the eigenstrain of the r-th HPV can be determined from the crystallographic theory as:

$$\varepsilon_{ij}^{tr,r} = \frac{1}{2}\left(b_i^r m_j^r + b_j^r m_i^r\right), \quad r = 1, .., 24. \tag{1}$$

The superscript »*tr*« in (1) implies that this strain is a consequence of the martensitic transformation and can also be called transformation strain.

The derivation of constitutive equations can be done within the scope of irreversible thermodynamics and the concept of materials with internal variables [35, 36]. Within this theory the thermodynamic state of a material is completely determined by a set of external (i.e. those that can be observed) and internal state variables. In our case the external variables are stress and temperature while the internal variables are the volume fractions of each HPV of martensite. Volume fractions are defined as

$$f^r = \frac{V^r}{V}, \qquad r = 1,..,24, \tag{2}$$

where V^r is the total volume occupied by the r-th HPV of martensite and V is the volume of the crystal grain. The total fraction of martensite is therefore

* Indical notation is used throughout the article, where lower indices are tensorial and upper indices denote the number of variant, the number of iteration or load step.

$$f = \sum_{r=1}^{24} f^r \tag{3}$$

and the following limits apply

$$0 \le f^r \le 1,\ r = 1, .., 24 \quad \text{and} \quad 0 \le f \le 1. \tag{4}$$

To characterize a material an expression for a thermodynamic potential as a function of state variables must be derived. In our case the thermodynamic potential is chosen to be the Gibbs energy. With the assumption of homogeneous temperature distribution and isotropic properties the expression for the Gibbs free energy of a single crystal of a SMA is [11, 37]:

$$\psi = \frac{1}{2}\sigma_{ij} S_{ijkl} \sigma_{kl} + \sigma_{ij} E_{ij}^{tr} - B(T - T_0) f - \frac{1}{2}\sum_{r=1}^{24} f_r \sum_{p=1}^{24} H^{pr} f_p \,, \tag{5}$$

where σ_{ij} is the volume average stress tensor and S_{ijkl} is the compliance tensor which can be constant as in [11] or can vary with transformation evolution as in [37]. If different elastic properties in martensite and austenite are assumed, a simple rule of mixture can be used to determine the actual compliance tensor during transformation

$$S_{ijkl} = (1 - f) S_{ijkl}^A + f S_{ijkl}^M, \tag{6}$$

where S_{ijkl}^A is the compliance tensor of a completely austenitic material ($f = 0$) and S_{ijkl}^M is the compliance tensor of a completely martensitic material ($f = 1$). In (5) E_{ij}^{tr} is the average transformation strain tensor and is defined as

$$E_{ij}^{tr} = \sum_{r=1}^{24} f^r \varepsilon_{ij}^{tr,r} \,. \tag{7}$$

The third term in (5) is the contribution due to the difference in chemical free energy of martensite and austenite. Equilibrium temperature T_0 is the temperature where the chemical free energies of both phases are equal. If there were no non-chemical contributions to the total Gibbs free energy the forward and reverse transformation would both take place at constant temperature T_0. However, due to non-chemical contributions forward and reverse transformation start at different temperatures and are not isothermal processes. If the temperature M_S of start of forward transformation in unloaded sample and the temperature A_F of finish of the reverse transformation are known, T_0 can be estimated from the following equation [38]:

$$T_0 = \frac{A_F + M_S}{2} \,. \tag{8}$$

In the vicinity of T_0 it is assumed that the difference in chemical energy is linear with temperature T. Coefficient B is a material parameter that defines the linear dependency. In practice, B describes the dependency of the critical stress for the onset of the stress induced transformation on temperature. The last term in (5) is the contribution due to the interaction between different HPVs. Namely, with creation and growth of each HPV a stress field is created that can either promote or obstruct the growth of other variants. This influence is captured in a 24x24 matrix H^{pr}.

The driving force for the transformation of the r-th HPV is determined by the equation

$$F^r = \frac{\partial \psi}{\partial f^r} = \frac{1}{2}\sigma_{ij} \Delta S_{ijkl} \sigma_{kl} + \sigma_{ij} \varepsilon_{ij}^{tr,r} - B(T - T_0) - \sum_{p=1}^{24} H^{pr} f^p \,, \tag{9}$$

where $\Delta S_{ijkl} = S_{ijkl}^M - S_{ijkl}^A$. Note that the first term in (9) was neglected in [12] although non-constant elastic properties were later taken account in the Hooke's law (11).

For martensite to grow inside austenite, the interface between the two must move. The movement of the interface is not frictionless, therefore dissipation occurs during growth of martensite. Taking into account the second law of thermodynamics results in the fact that for the transformation to proceed the driving force must reach a certain critical force F^c. It is assumed that the critical force does not change during the transformation, resulting in

the consistency equation $F^r = F^c$ if forward transformation is in progress on variant r, or $F^r = -F^c$ for reverse transformation (we assume resistance to moving interface is equal regardless of the direction of movement). It should also be noted that state when $F^r > F^c$ is physically inconsistent.

From the definition of the Gibbs energy the equation for the total strain tensor follows as

$$E_{ij} = \frac{\partial \psi}{\partial \sigma_{ij}} = S_{ijkl}\sigma_{kl} + E_{ij}^{tr}. \tag{10}$$

Eq. (10) can be written more familiarly in the form of the Hooke's law

$$\sigma_{ij} = C_{ijkl}\left(E_{kl} - E_{kl}^{tr}\right), \tag{11}$$

where C_{ijkl} is the stiffness tensor ($C_{ijkl} = S_{ijkl}^{-1}$) and $E_{kl} - E_{kl}^{tr}$ can be identified as the elastic part of the strain tensor so the total strain tensor can be expressed as

$$E_{ij} = E_{ij}^{el} + E_{ij}^{tr}. \tag{12}$$

As will be shown in the next chapter, it is necessary to explicitly express the dependence of the stiffness tensor on the martensite volume fraction. The expression for C_{ijkl} can be derived from (6) with additional assumption that elastic properties of martensite and austenite differ only by a factor a, that is $S_{ijkl}^M = aS_{ijkl}^A$. If isotropy is assumed factor a is equal to the coefficient of Young's modulus of austenite divided by the modulus of martensite. Eq. (6) can now be rewritten as

$$S_{ijkl} = (1 - f + fa)S_{ijkl}^A.$$

Taking into account $C_{ijkl}^A = \left(S_{ijkl}^A\right)^{-1}$ we arrive at the following expression

$$C_{ijkl} = \frac{1}{1 - f + fa}C_{ijkl}^A. \tag{13}$$

3 Numerical modelling

3.1 Single crystal equilibrium

The problem of the local equilibrium of a single crystal can be solved incrementally with implicit method (backward Euler integration) which gives us a structure of return mapping algorithms. By using implicit method bigger load steps can be used without loss of accuracy or convergence problems. The total load is divided into finite number of load steps. The reference state is an unloaded completely austenitic crystal at temperature T (f^r=0, r=1, .., 24, E_{ij}=0). Values $\sigma_{ij}^n, f^{r,n}$, r = 1, .., 24 at load step n and the total strain E_{ij}^{n+1} at step n+1 are known and the unknown values $\sigma_{ij}^{n+1}, f^{r,n+1}$, r = 1, .., 24 at step n+1 must be calculated. Following steps must be taken:

1. Totally elastic response is assumed in order to calculate a trial value of the stress tensor:

   $$\sigma_{ij}^{n+1,trial} = C_{ijkl}^n\left(E_{kl}^{n+1} - E_{kl}^{tr,n}\right),$$

   where

   $$C_{ijkl}^n = \frac{1}{1 - f^n + f^n a}C_{ijkl}^A.$$

2. It must be checked whether the transformation condition F^r=$F^{c\dagger}$ is met by calculating a trial driving force for each variant r = 1, .., 24 (in the following equation load step index is omitted for clarity):

† Here only the forward transformation is considered. Analogy applies for the derivation in the case of reverse transformation, where of course condition $F^r = -F^c$ is checked.

$$F^{r,trial} = \frac{1}{2}\sigma_{ij}^{trial}\Delta S_{ijkl}\sigma_{kl}^{trial} + \sigma_{ij}^{trial}\varepsilon_{ij}^{tr,r} - B(T - T_0) - \sum_{p=1}^{24} H^{pr} f^{p,n} \cdot$$

In general it cannot be expected that condition $F^{r,trial}=F^c$ will be met exactly. If for all variants r = 1,.., 24 $F^{r,trial}<F^c$ there is no transformation in progress. Hence, the response is totally elastic and no further calculation is necessary and next load step can be applied since in this case the trial state is actually the physically correct state. If such r exists that $F^{r,trial}>F^c$ then our trial state is physically inconsistent. A set of active variants Γ including all variants for which $F^{r,trial}>F^c$ is created:

$$\Gamma = \{r \,|\, F^{r,trial} > F^c, r = 1,..,24\}$$

before proceeding to step 3 to fix this state.

3. The new stress tensor σ_{ij}^{n+1} is expressed with trial values. Combining (11), (13) and (7) the updated stress tensor can be expressed as:

$$\sigma_{ij}^{n+1} = \frac{1}{1 - f^{n+1} + f^{n+1}a} C_{ijkl}^{A}\left(E_{kl}^{n+1} - \sum_r f^{r,n+1}\varepsilon_{kl}^{tr,r}\right), \tag{14}$$

where changes in volume fractions $\Delta f^{r,n+1}$, r = 1, ..,24, are defined from

$$f^{r,n+1} = f^{r,n} + \Delta f^{r,n+1}, \qquad r = 1,..,24 .$$

In the following derivation it is desirable to acquire equations that are linearly dependent on changes in volume fractions. To achieve this and without sacrificing much accuracy (assuming that load steps are not too big and factor a is not extremely big) Eq. (13) is linearized around f^n:

$$C_{ijkl}^{n+1} = C_{ijkl}^{n} + \frac{dC_{ijkl}^{n}}{df^{n}}\Delta f^{n+1} = C_{ijkl}^{n} + \frac{1-a}{\left(1 - f^{n} + f^{n}a\right)^2} C_{ijkl}^{A}\sum_{r\in\Gamma}\Delta f^{r,n+1} \cdot$$

Eq. (14) now becomes

$$\begin{aligned}\sigma_{ij}^{n+1} &= \left(C_{ijkl}^{n} + b^n C_{ijkl}^{A}\sum_{r\in\Gamma}\Delta f^{r,n+1}\right)\left(E_{kl}^{n+1} - E_{kl}^{tr,n} - \sum_{r\in\Gamma}\Delta f^{r,n+1}\varepsilon_{kl}^{tr,r}\right) = \\ &= \sigma_{ij}^{n+1,trial} - C_{ijkl}^{n}\sum_{r\in\Gamma}\Delta f^{r,n+1}\varepsilon_{kl}^{tr,r} + b^n C_{ijkl}^{A}\left(E_{kl}^{n+1} - E_{kl}^{tr,n}\right)\sum_{r\in\Gamma}\Delta f^{r,n+1} - b^n C_{ijkl}^{A}\sum_{r\in\Gamma}\Delta f^{r,n+1}\sum_{r\in\Gamma}\Delta f^{r,n+1}\varepsilon_{kl}^{tr,r}\end{aligned}, \tag{15}$$

where for clarity factor b^n is introduced as

$$b^n = \frac{1-a}{\left(1 - f^{n} + f^{n}a\right)^2} \cdot$$

If load steps of reasonable size are used it is acceptable to neglect the term quadratic in Δf^r in (15). Combining (9) and (15) the driving force at step n+1 can be expressed as:

$$\begin{aligned}F^{r,n+1} &= \Delta S_{ijkl}\left(\sigma_{ij}^{n+1,trial} - C_{ijpq}^{n}\sum_{m\in\Gamma}\Delta f^{m,n+1}\varepsilon_{pq}^{tr,m} + b^n C_{ijpq}^{A}\left(E_{pq}^{n+1} - E_{pq}^{tr,n}\right)\sum_{m\in\Gamma}\Delta f^{m,n+1}\right) * \\ &* \left(\sigma_{kl}^{n+1,trial} - C_{klpq}^{n}\sum_{m\in\Gamma}\Delta f^{m,n+1}\varepsilon_{pq}^{tr,m} + b^n C_{klpq}^{A}\left(E_{pq}^{n+1} - E_{pq}^{tr,n}\right)\sum_{m\in\Gamma}\Delta f^{m,n+1}\right) + \\ &+ \sigma_{ij}^{n+1,trial}\varepsilon_{ij}^{tr,r} - C_{ijkl}^{n}\left(\sum_{m\in\Gamma}\Delta f^{m,n+1}\varepsilon_{kl}^{tr,m}\right)\varepsilon_{ij}^{tr,r} + \left(b^n C_{ijkl}^{A}\left(E_{kl}^{n+1} - E_{kl}^{tr,n}\right)\sum_{m\in\Gamma}\Delta f^{m,n+1}\right)\varepsilon_{ij}^{tr,r} - \\ &- B(T - T_0) - \sum_{m\in\Gamma} H^{rm} f^{m,n} - \sum_{m\in\Gamma} H^{rm}\Delta f^{m,n+1}\end{aligned} .$$

For all $r \in \Gamma$ the condition $F^{r,n+1}=F^c$ is enforced which results in a nonlinear system of equations with only unknowns being $\Delta f^{r,n+1}, r \in \Gamma$. The system can be solved by Newton-Rhapson method with initial values set to zero.

4. The solution from step 3 must be checked for physical consistency, i.e. if forward transformation is in progress all values $\Delta f^{r,n+1}, r \in \Gamma$ should be positive. If there are $\Delta f^{r,n+1}, r \in \Gamma$ with negative values, the most negative is eliminated from the active variants set [29] and a new set Γ is defined:

$$\Gamma = \Gamma - \{r \left| \Delta f^{r,n+1} = \min\left(\Delta f^{r,n+1} \right| r \in \Gamma\right)\}.$$

The algorithm now returns to step 3 to calculate new values $\Delta f^{r,n+1}, r \in \Gamma$. If there are no negative values it proceeds to step 5.

5. Updated stress tensor σ_{ij}^{n+1} is calculated from (15) and then the updated driving forces $F^{r,n+1}$, r = 1, .., 24. It might happen that some of the newly calculated driving forces are physically inconsistent, i.e. $F^r > F^c$. If this occurs the variant with the most positive driving force is added to the set of active variants:

$$\Gamma = \Gamma \cup \{r \left| F^{r,n+1} = \max\left(F^{r,n+1} \right| r \notin \Gamma; F^{r,n+1} > F^c\right)\}$$

and algorithm returns to step 3 to calculate new values $\Delta f^{r,n+1}, r \in \Gamma$ on this new set. During our calculations it proved useful not to add new variants to the set in the first Newton iteration of the global FEM equation solution (explained below), since the prediction of the active variants set from the trial state is in general correct, but can be distorted due to local imbalance that occurs after updating the stress at each Gauss point. Furthermore, it also proved useful to set a tolerance for the difference F^r-F^c based on the current error of the global FEM iteration (residual of (17)). That is if the error is still very large a variant is added to the set only if the difference F^r-F^c is greater than half of the error. When error is less than 10^{-5} a new variant is added, no matter how big the difference F^r-F^c is (as long as it is positive). If there are no variants for which $F^r > F^c$ algorithm proceeds to the next load step (n+2).

6. It should be noted that some variants that were eliminated in step 4 can be re-added in step 5 [33]. This can lead to an infinite loop in the algorithm. To prevent this, the following safety mechanism is included: if step 5 is repeated more than 24 times the load step is divided by two and the calculation is repeated from step 1. During our calculations this proved to be an effective mechanism for achieving convergence of the algorithm.

3.2 Polycrystal modelling

Polycrstals are modeled with the finite element method where each finite element represents a crystal grain. The orientation of each grain is defined by three Euler angles (ϕ,ϑ,ρ). The standard x-convention [39] is used to define the angles as is shown on Fig. 5. The matrix for transformation from local (crystal grain) to global (polycrystal) coordinate system is:

$$\mathbf{T}(\phi,\vartheta,\rho) = \begin{bmatrix} \cos\phi\cos\rho - \cos\vartheta\sin\phi\sin\rho & \sin\phi\cos\rho + \cos\vartheta\cos\phi\sin\rho & \sin\vartheta\sin\rho \\ -\cos\phi\sin\rho - \cos\vartheta\sin\phi\cos\rho & -\sin\phi\sin\rho + \cos\vartheta\cos\phi\cos\rho & \cos\rho\sin\vartheta \\ \sin\vartheta\sin\phi & -\sin\vartheta\cos\phi & \cos\vartheta \end{bmatrix}$$

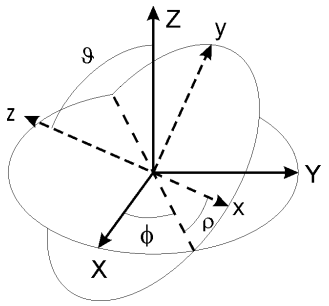

Fig. 5 Definition of the Euler angles used to determine the orientation of the local coordinate system (xyz) in the global coordinate system (XYZ).

For the construction of the global FEM equation it is necessary that parameters and variables of all the elements are expressed in the global coordinate system. Therefore, when solving local equations in finite elements (i.e. crystal grains) the habit plane vectors must be transformed with the Euler transformation matrix prior to performing any calculation. Next, the equations of the RVE are solved at each Gauss point of finite elements by the algorithm presented in chapter 3.1, thereby achieving local equilibrium. Global equilibrium (equilibrium of the finite element mesh) is achieved iteratively by balancing internal and external forces. Our problem is formulated as strain driven, therefore displacements (u_i) of all the nodes must be determined first from the global FEM equation for the trial (i.e. elastic) state. With known displacements the total strain tensor is determined from the linear strain equation:

$$E_{ij} = \frac{1}{2}\left(u_{i,j} + u_{j,i}\right). \tag{16}$$

Strain from (16) is then our input into the algorithm from chapter 3.1 and the output are the stress tensor and updated martensite volume fractions at each Gauss point. Based on the calculated stresses the internal forces in our finite element model can be calculated (see e.g. [40] for details). For structures in equilibrium this forces should be equal to external forces (loads), that is:

$$F_i^{ext} - F_i^{\text{int}} = 0, \tag{17}$$

where F_i^{int} and F_i^{ext} are vectors of internal and external forces (not to be confused with the driving force), consecutively and their dimensions are the number of degrees of freedom of the finite element model . Eq. (17) is actually a system of nonlinear equations in u_i since $F_i^{\text{int}} = F_i^{\text{int}}\left(u_j\right)$, which can again be solved by the Newton-Rhapson method if the jacobian can be calculated. Following the procedures of the nonlinear finite element method (see e.g. [40]) it can be shown that the jacobian can be calculated if we can find the derivative of stress tensor with respect to strain tensor. From (15) it follows:

$$\frac{\partial \sigma_{ij}^{n+1}}{\partial E_{kl}} = C_{ijkl}^{n} - C_{ijmn}^{n}\sum_{r\in\Gamma}\frac{\partial \Delta f^{\,r,n+1}}{\partial E_{kl}}\varepsilon_{mn}^{tr,r} + \left(C_{ijmn}^{M} - C_{ijmn}^{A}\right)\left(E_{mn}^{n+1} - E_{mn}^{tr,n}\right)\sum_{r\in\Gamma}\frac{\partial \Delta f^{\,r,n+1}}{\partial E_{kl}} + \left(C_{ijkl}^{M} - C_{ijkl}^{A}\right)\sum_{r\in\Gamma}\Delta f^{\,r,n+1}. \tag{18}$$

To evaluate (18) the derivative of martensite volume fraction increment with respect to strain tensor must be found. By taking into account that the driving force is constant during transformation and taking partial derivative of (9) with respect to strain tensor we get the following equation:

$$\frac{\partial F^{\,r,n+1}}{\partial E_{kl}} = \frac{\partial \sigma_{ij}^{n+1}}{\partial E_{kl}}\left(\Delta S_{ijmn}\sigma_{mn} + \varepsilon_{ij}^{tr,r}\right) - \sum_{p=1}^{24} H^{\,pr}\,\frac{\partial \Delta f^{\,p,n+1}}{\partial E_{kl}} = 0, \qquad r \in \Gamma. \tag{19}$$

Inserting (18) in (19) results in a system of linear equations for $\frac{\partial \Delta f^{\,r,n+1}}{\partial E_{kl}}$ the solution of which can be back substituted into (18) hence enabling us to determine the jacobian exactly which is important for the quadratic convergence of the global FEM equation (17).

During calculations additional caution has to be taken to check if martensite volume fractions are within limits given by (4). Usually there is more than one variant active in an element and volume fraction of the element

will reach 1 before a single variant will break this limit. Therefore, it is reasonable to control the total volume fraction of martensite in elements rather than fractions of each variant separately. After the FEM has converged (residual of (17) is less than tolerance) each element is checked and if martensite fraction is greater than 1 minus some tolerance the load step is divided into two substeps and the FEM calculation is repeated with this smaller step. If a model consists of many elements this sub-stepping algorithm can take a long time to converge, so it is recommendable not to choose to tight a tolerance (we set it to 10^{-2}).

The complete numerical algorithm involving FEM can be summarized in the following steps:

1. Mesh the model with finite elements.
2. Define the internal orientation of each finite element by means of Euler angles.
3. Transform transformation parameters from local to global coordinate system.
4. Apply next increment of load if total load is not reached yet.
5. Calculate trial (elastic) state, i.e. solve linear FEM problem to determine initial displacements.
6. Determine strain at each Gauss point from displacements.
7. Based on calculated strain from step 6 perform return mapping algorithm (chapter 3.1) at each Gauss point of each element.
8. Calculate the residual of (17) (i.e. determine internal forces from stresses obtained in step 7). If residual is less than the set tolerance, update stresses and martensite volume fractions. Check if martensite fractions are within the limits. If they are return to step 4. If any limit for martensite fraction is violated divide the current load step by two return all variables to the values of last converged (sub)step and return to step 4.
9. Calculate the jacobian from (18) and the displacement increment from the Newton-Rhapson method. Calculate updated displacement and return to step 6.

4 Results and discussion

4.1. Experimental techniques and determination of material parameters

To perform calculations with the presented model the following material parameters must be input:

- elastic properties of both phases (C^A_{ijkl}, C^M_{ijkl})
- F^c – critical driving force
- T_0 – equilibrium temperature
- texture data (orientations of crystal grains)
- crystallographic parameters of the 24 HPVs (b^r_i, m^r_i, r = 1, .., 24)
- B – coeffiecient of linear dependency of chemical energy around equilibrium temperature
- interaction matrix H^{pr}

Ideally, all of the parameters (except texture) should be determined by experiments on single crystals. However, we were unable to obtain monocrystalline samples of Ni-Ti as they are very difficult to produce. Therefore, some deductions based on experimental results on polycrystals were made that enabled the determination of the missing parameters. Polycrystalline samples in form of superelastic wires were obtained from a commercial source. The composition of the alloy as given by the manufacturer was 50.8 at.% Ni and Ti balance. The diameter of the wire was 3 mm and the length was 200 mm. We had access to a Zwick Z050 universal testing machine and a Netzsch DSC 204 F1 differential scanning calorimetry (DSC) apparatus. Tensile tests on wires were conduced with position load control and the speed of loading ($\dot{\varepsilon}$) was 10^{-4} s^{-1} in order to reduce the thermal coupling effect during transformation. Temperature control was achieved by confining the sample and the grips during the tensile test in a ventilated temperature chamber. To determine tension-compression asymmetry compression tests were made on the tensile samples which were cut to a length of approx. 57 mm. To prevent samples from buckling special guides were constructed as shown on Fig. 6. The guides enabled the use of compression extensometers which require a minimum clearance of 25 mm.

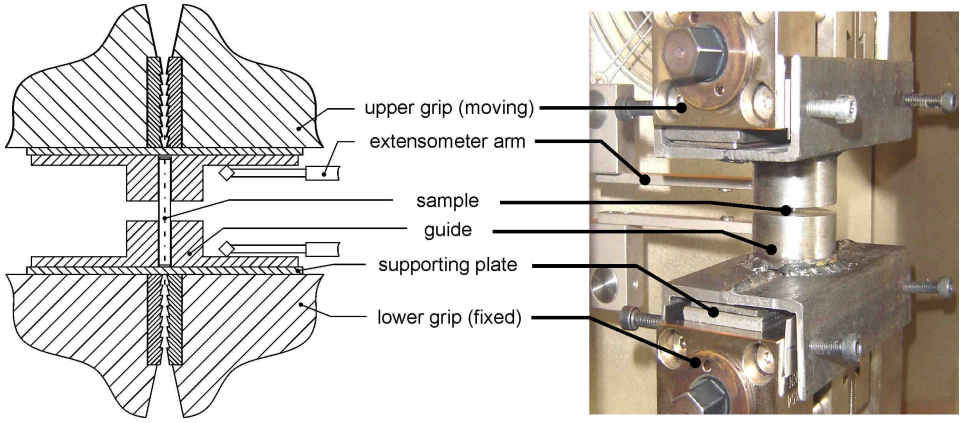

Fig. 6 Experimental setup for compression tests

DSC tests were carried out on samples cut from wires with abrasive water jet. The samples for DSC analysis were approximately 3 mm in height. The speed of heating and cooling during the test was 10 $Kmin^{-1}$. From the results of the DSC analysis the transformation temperatures were determined as follows: A_F = 306 K, A_S = 268 K, M_S = 234 K and M_F = 205 K. From (8) it follows T_0 = 270 K.

If isotropy is assumed only Young's modulus and Poisson's ratio of both austenitic and martensitic phase should be measured to determine elastic properties. Our material was austenitic at room temperature, so Young's modulus can readily be determined from the initial tangent during the tensile experiments. Poisson's ratio was not measured and was assumed to be equal in austenite and martensite and the value vas set at $\nu = 0.3$ as suggested in literature [8]. The measurement of martensite's Young's modulus should be conducted at a temperature where material is completely martensitic. We were not able to reach such a low temperature so we estimated the martensitic modulus from the tangent of unloading after loading to a level where stress-induced martensitic transformation was completed (Fig. 7). The unloading curve is non-linear since inelastic effects such as martensite variants' reorientation and reverse transformation in some grains take place during unloading. In general the highest measured value for modulus (tangent) should be taken as the real modulus of martensite [41].

Assuming that F^c is a material constant it can be shown that the area of a hysteresis loop obtained in a closed transformation cycle in isothermal load-displacement experiment is always equal to $2F^c$ [10]. We determined F^c from a uniaxial tensile experiment on a wire at different temperatures. As seen from Table 1 there is no significant difference for values determined at different temperatures. In our calculations we use the value F^c = 9.7 MPa. Fig. 7 shows the experimental stress-strain curve obtained at 313 K and the area used to calculate F^c is shown.

Temperatue [K]	F^c [MPa]
303	9.9
313	9.7
323	9.7

Table 1 Critical driving force for transformation as determined from the hysteresis area at different temperatures.

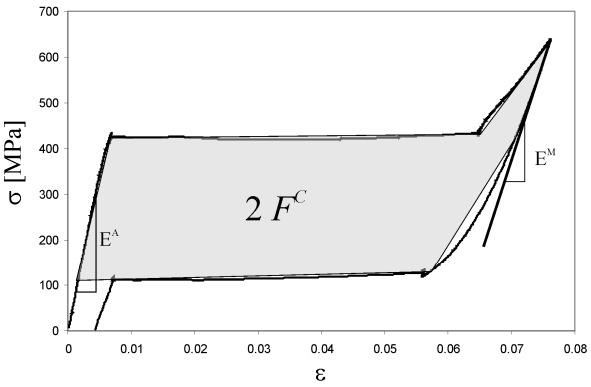

Fig. 7 Determination of Young's modulus of both phases and the approximate area used to calculate F^c.

Texture of the specimens can be measured by X-ray diffraction or EBSD (electronic back scatter diffraction) analysis. Unfortunately, we were not able to conduct any of the two methods, therefore we determined orientations of the crystal grains in our model under the assumption that during the wire production process plastic slip occurs on the <111>{110} system (typical for materials with BCC lattice). This is consistent with the texture experimentally determined in [12] and [30]. Pole figures of the texture for 343 grains used in our calculations are shown on Fig. 8. Note that the center of the pole figure coincides with the direction of the loading which is also the direction of the wire drawing.

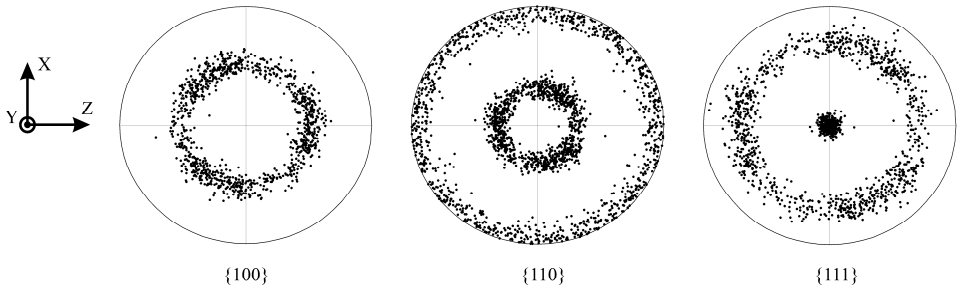

Fig. 8 Pole figures showing the asumed texture used in calculations.

Theoretical predictions of the crystallographic parameters are in good accordance with the known experimental results [20], therefore these predictions are used in our model. As mentioned the crystallographic parameters are alloy specific and can be calculated if the lattice parameters of both phases are known. In literature the closest composition with measured lattice parameters is an alloy with 51.9 at. % Ni [42] and this data is used to calculate the HPV parameters which are given in Table 2.

Table 2 HPV parameters for the 24 variants used in our calculations.

	$m_1 = 0.8881$ $m_2 = 0.4038$ $m_3 = 0.2196$	$b_1 = 0.0574$ $b_2 = 0.0627$ $b_3 = 0.0963$			
Variant	**m**	**b**	Variant	**m**	**b**
1	$(-m_1, -m_2, m_3)$	$(b_1, -b_2, b_3)$	13	$(-m_3, m_1, -m_2)$	$(-b_3, -b_1, -b_2)$
2	$(-m_2, -m_1, -m_3)$	$(-b_2, b_1, -b_3)$	14	$(-m_3, -m_1, m_2)$	$(-b_3, b_1, b_2)$
3	(m_1, m_2, m_3)	$(-b_1, b_2, b_3)$	15	$(m_3, m_2, -m_1)$	(b_3, b_2, b_1)
4	$(m_2, m_1, -m_3)$	$(b_2, -b_1, -b_3)$	16	$(m_3, -m_2, m_1)$	$(b_3, -b_2, -b_1)$
5	$(-m_1, m_2, -m_3)$	$(b_1, b_2, -b_3)$	17	$(m_1, -m_3, m_2)$	$(-b_1, -b_3, b_2)$
6	$(m_2, -m_1, m_3)$	(b_2, b_1, b_3)	18	$(-m_1, -m_3, -m_2)$	$(b_1, -b_3, -b_2)$
7	$(m_1, -m_2, -m_3)$	$(-b_1, -b_2, -b_3)$	19	(m_2, m_3, m_1)	$(b_2, b_3, -b_1)$
8	$(-m_2, m_1, m_3)$	$(-b_2, -b_1, b_3)$	20	$(-m_2, m_3, -m_1)$	$(-b_2, b_3, b_1)$
9	(m_3, m_1, m_2)	$(b_3, -b_1, b_2)$	21	$(m_1, m_3, -m_2)$	$(-b_1, b_3, -b_2)$
10	$(m_3, -m_1, -m_2)$	$(b_3, b_1, -b_2)$	22	$(-m_1, m_3, m_2)$	(b_1, b_3, b_2)
11	$(-m_3, -m_2, -m_1)$	$(-b_3, -b_2, b_1)$	23	$(-m_2, -m_3, m_1)$	$(-b_2, -b_3, -b_1)$
12	$(-m_3, m_2, m_1)$	$(-b_3, b_2, -b_1)$	24	$(m_2, -m_3, -m_1)$	$(b_2, -b_3, b_1)$

The parameter B can be exactly determined only on single crystals. However a strategy from [12] can be used to estimate B from results of tensile tests of polycrystal specimens with known texture at different temperature. Namely, assuming uniaxial stress state it follows from (9) that when the transformation starts ($f = 0$) the following equation holds

$$\frac{1}{2}\left(\sigma^{cr}\right)^2 \Delta S_{1111} + \sigma^{cr}\varepsilon^{tr,\max} - B\left(T - T_0\right) = F^c,$$

where σ^{cr} is the critical stress needed for the onset of the transformation at given T and $\varepsilon^{tr.\max}$ is the transformation strain of the HPV variant with the maximum value. If the difference in elastic properties is neglected it can be deducted that

$$B = \frac{\partial \sigma^{cr}}{\partial T} \varepsilon^{tr,\max}, \tag{20}$$

meaning that B can be determined if critical stress for the onset of transformation is measured at different temperatures. Based on the assumed texture the following estimation can be made: we assume that the polycrystal is acting very much like a single crystal oriented in the [111] direction. For [111] direction $\varepsilon^{tr.\max} = 0.053$. Table 3 shows the values of critical stress at different temperature as determined from tensile experiments. From this data average stress rate $\left(\frac{\partial \sigma^{cr}}{\partial T}\right)$ can be determined to be 7.6 MPa/K and from (20) it follows $B = 0.4$ MPa/K.

Temperature [K]	σ^{cr} [MPa]
299	315
303	355
313	420
323	500
333	580

Table 3 Temperature dependence of critical stress for forward transformation.

The interaction matrix H^{pr} is practically impossible to measure. It can be estimated by micromechanical analysis (see e.g. [43]) but for Ni-Ti the values of the matrix elements are very low. Therefore, we neglect the interaction energy, i.e. $H^{pr} = 0$, p, r = 1, .., 24. Material properties used in our calculations are summarized in Table 4.

Table 4 Determination of material properties**.**

Material property	Method of determination	Value used in our calculations
Young's modulus of austenite E^A	from uniaxial tensile test	67 GPa
Young's modulus of austenite E^M	from uniaxial tensile test (tangent at unloading after complete transformation)	30 GPa
Poisson's ratio of austenite and martensite ν	from literature [8]	0.3
Critical driving force F^c	measurement of hysteresis area at full transformation cycle	9.7 MPa
Thermodynamic equilibrium temperature T_0	arithmetic mean of austenite finish and martensite start temperature, which are measured by DSC	270 K
Crystallographic texture	based on characteristics of sample production technology and data in literature [12, 30]	<111>{110} texture
Crystallographic parameters of HPV b_i^r, m_i^r, r = 1, ..,24	theoretical prediction based on crystallographic theory of martensite transformation	see Table 2
Coefficient of linear dependency B	estimated from temperature dependence of critical stress for transformation for assumed texture	0.4 MPa/K
Interaction matrix H^{pr}	theoretical prediction based on micromechanical analysis	$H^{pr} = 0$, p, r = 1, .., 24 (neglected)

4.2. Performance of the numerical model and comparison to experimental results

The algorithm presented in chapter 3 was converted to FORTRAN code. Standard finite element procedures were implemented using libraries presented in [44]. Geometrically our model was a cube divided into 8-node cubic elements, 7 elements on each side, totaling in 343 elements for the whole model. The number of elements was chosen relatively low in order to be able to make calculations on a standard personal computer in reasonable time. As suggested in [12, 31] 343 elements are sufficient to give reasonable enough results in terms of macroscopic stress-strain behaviour and texture representation. One face of the model had displacements constraints in the direction of loading (in our case y-axis). Additionally two edges of the restrained face had additional constraints in all directions in order to prevent rigid body rotation. On the face opposite to the restrained face loadings in form of displacements were applied. Results for the stress-strain curve were obtained by graphing the total displacement of the loaded face vs. the resultant force load on the same face (obtained by summing resultant forces of all nodes on the face). The geometry of the FEM model, the constraints and loading conditions are depicted in Fig. 9.

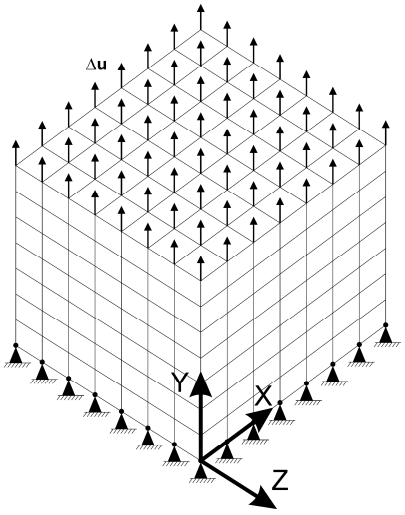

Fig. 9 FEM model used in our calculations consists of 343 8-node cubic elements, bottom face is constrained and top face is loaded with displacements.

Taking into account the implicit nature of the presented algorithm relatively large load steps can be chosen. However, if steps are too big convergence problems may occur due to the fact that the number of active martensite variants between two Newton iterations of the FEM algorithm changes significantly. The larger the mesh (with more elements) the more variants are potentially activated, hence larger meshes require smaller load steps. The model with 343 elements converged if 50 or more load steps were used for loading up to the total strain of 0.08. The same number of steps was used for the unloading. For the given setup the calculation time was about 24 hrs on a PC with E8500 Intel processor (with only one core used) and 4 GB RAM. A typical convergence during a load step is shown in Table 5. It can be noted that globally the convergence is not quadratic which can be attributed to the fact that number of active variants changes from one iteration to another. Once the number of active variants is stabilized the convergence is fast.

Table 5 Convergence for a typical load step in simulation of a polycrystal with 343 grains.

Iteration	Residual of (17)	Total number of active variants in the polycrystal
1	2.9180967	6797
2	$1.3196692 \cdot 10^{-2}$	6792
3	$3.2286778 \cdot 10^{-2}$	6876
4	$4.9763587 \cdot 10^{-5}$	6875
5	$1.1723609 \cdot 10^{-3}$	6883
6	$1.6483625 \cdot 10^{-8}$	6883
7	$1.2520009 \cdot 10^{-14}$	6883

Figs. 10-12 show the comparison of the experimental and numerical data for tension at three different test temperatures. The results of the numerical analysis are in general in good agreement with the experimental results. The stress plateau level is predicted well although the quality of prediction depends on temperature. This can be attributed to the fact that the value of parameter *B* is not determined exactly by measurements on single crystals. The prediction of the maximum transformation strain is also good but significant differences arise after the transformation ends. Experimental results imply that after the austenite to martensite transformation is complete the response is not completely elastic as assumed in the model. The reason for inelastic response lies in the reorientation and detwinning of martensite variants, which can not be captured with the existing model which is based on habit plane variants (twinned martensite) rather than on correspondence variants (single martensite variants). The same reason causes inelasticities in martensite unloading which makes the determination of martensitic Young's modulus difficult. Nevertheless, the average slopes of the martensite unloading in the numerical model and experimental results are in good agreement. It can also be observed that the strain in experimental samples does not recover completely. This is caused by local plastic deformation and by incomplete reverse transformation (areas of martensite stay trapped inside austenite). Neither of these effects is covered in the presented model and complete recovery is predicted. These effects should be taken into account if cyclic loading is to be studied. Namely, in subsequent cycles the residual strain accumulates and the error of prediction increases with each cycle.

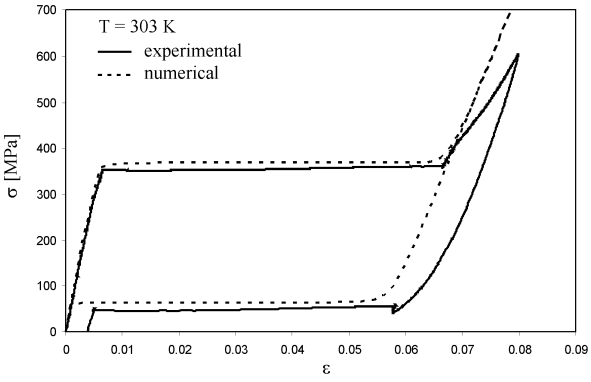

Fig. 10 Comparison of experimental and numerical results at 303 K.

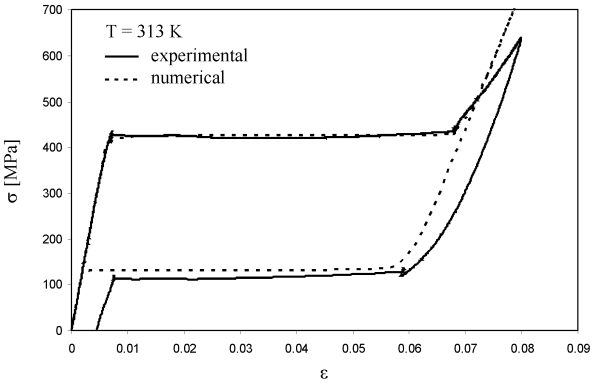

Fig. 11 Comparison of experimental and numerical results at 313 K.

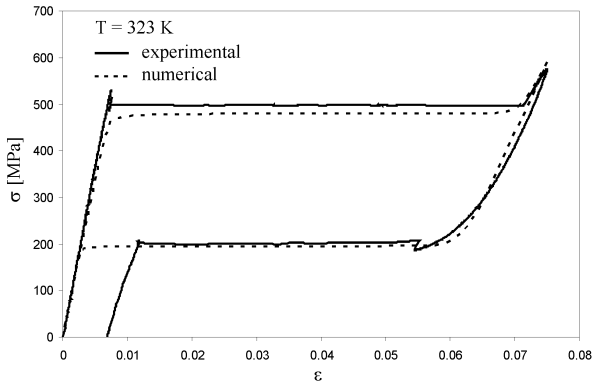

Fig. 12 Comparison of experimental and numerical results at 323 K.

Fig. 13 shows the comparison of numerical results to results of compression tests. The agreement is much worse than in case of tension. However, the general tendency of higher transformation stress plateau and smaller maximum transformation strain is predicted. As can be observed the experimental hysteresis for a complete cycle is greater than in tension. This can be attributed to the effects of sample constraining in the guides which could not be made completely frictionless. Also significant indentation marks were left on the supporting plate (Fig. 6) indicating that it cannot be considered completely stiff which affects the slope of the stress-strain curve.

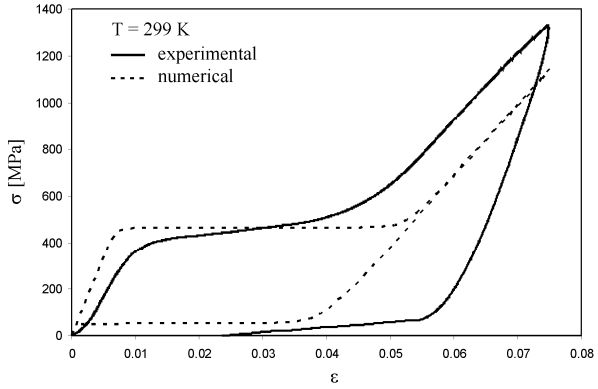

Fig. 13 Comparison of experimental and numerical results for compression.

To determine the effect of different elastic properties calculations with the presented model were made under assumption of equal elastic properties in austenite and martensite. Fig. 14 shows the comparison with the results obtained for different elastic properties. As can be observed, the transformation stress plateau level and maximum transformation strain are significantly affected by this assumption. The difference in maximum transformation strain is attributed to the difference in elastic strain of martensite due to different Young's modulus.

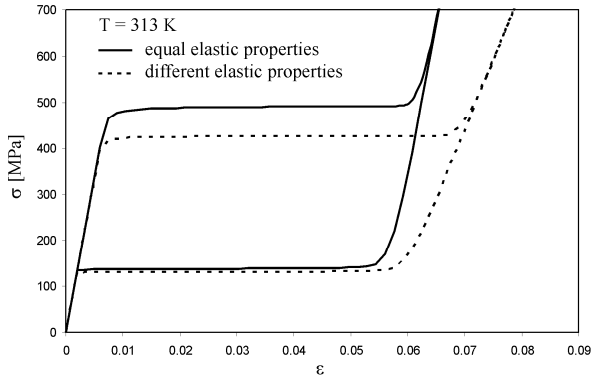

Fig. 14 Comparison of simulation results obtained with equal and different elastic properties in austenite and martensite.

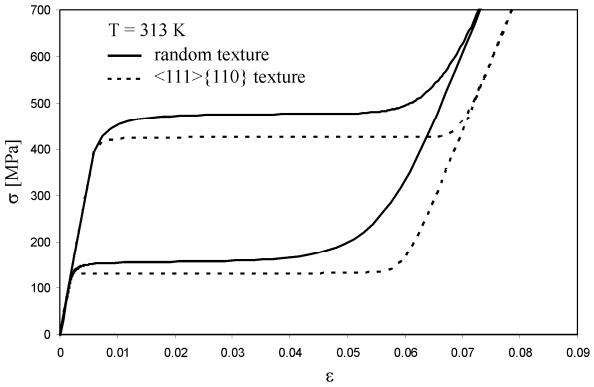

Fig. 15 Comparison of simulation results obtained for a polycrystal with a random texture and a polycrystal with strong <111>{110} texture

Fig. 15 shows the importance of texture for polycrystalline materials modelling. A significant difference in maximum transformation strain can be observed for a polycrystal with randomly assigned texture and a polycrystal with <111>{110} texture. As a consequence, stress plateau levels also differ, since the area of the hysteresis loop is constant.

5 Conclusions

A numerical algorithm for the solution of the constitutive equations based on micromechanics of SMA with different elastic properties in austenite and martensite was presented. The algorithm is based on an implicit scheme which reduces convergence problems. Nevertheless, load step size is limited mainly because of the active variants selection process. The use of small load steps during the entire calculation was prevented by application of a sub stepping algorithm.

Results of the numerical simulation were compared to experimentally obtained stress-strain curves on polycrystalline Ni-Ti wires. The comparison of stress plateau level, maximum transformation strain and temperature dependence showed good agreement of numerical and experimental data in tension. It was shown that the effect of non-constant elastic properties should not be neglected. Similarly, material texture plays a great role in the simulation of polycrystalline aggregates. Slightly worse agreement was observed in compression, but the overall

tendency of the tension-compression asymmetry was predicted well. To determine the reasons of worse agreement in compression more attention should be paid to the experimental setup. However, considering the amount of simplifications made in material parameter determination the results in general can be considered a good base for the following development of the model.

References

[1] L. C. Brinson, One Dimensional Constitutive Behavior of Shape Memory Alloys: thermo-mechanical derivation with non-constant material functions, J. Intel. Mat. Syst. Str. **4**, 229-242 (1993).
[2] F. Auricchio and J. Lubliner, A uniaxial model for shape-memory alloys, Int. J. Solids Struct. **34**, 3601-3618 (1997).
[3] S. Leclercq and C. Lexcellent, A general macroscopic description of the thermomechanical behavior of shape memory alloys, J. Mech. Phys. Solids **44**, 953-957 (1996).
[4] J. Rejzner, C. Lexcellent and B. Raniecki, Pseudoelastic behaviour of shape memory alloy beams under pure bending: experiments and modelling, Int. J. Mech. Sci. **44**, 665-686 (2002).
[5] F. Auricchio and E. Sacco, A Superelastic Shape-Memory-Alloy Beam Model, J. Intel. Mat. Syst. Str. **8**, 489-501 (1997).
[6] J. Lubliner and F. Auricchio, Generalized plasticity and shape memory alloys, Int. J. Solids Struct. **33**, 991-1003 (1996).
[7] M. Brocca, L. C. Brinson and Z. P. Bazant, Three-dimensional constitutive model for shape memory alloys based on microplane model, J. Mech. Phys. Solids **50**, 1051-1077 (2002).
[8] Y. Jung, P. Papadopoulos and R. O. Ritchie, Constitutive modelling and numerical simulation of multivariant phase transformation in superelastic shape-memory alloys, Int. J. Numer. Meth. Eng. **60**, 429-460 (2004).
[9] T. Bartel and K. Hackl, A micromechanical model for martensitic phase-transformations in shape-memory alloys based on energy-relaxation, Z. Angew. Math. Mech. **89**, 792-809 (2009).
[10] S. Stupkiewicz and H. Petryk, Modelling of laminated microstructures in stress-induced martensitic transformations, J. Mech. Phys. Solids **50**, 2303-2331 (2002).
[11] N. Siredey, E. Patoor et al., Constitutive equations for polycrystalline thermoelastic shape memory alloys.: Part I. Intragranular interactions and behavior of the grain, Int. J. Solids Struct. **36**, 4289-4315 (1999).
[12] P. Thamburaja and L. Anand, Polycrystalline shape-memory materials: effect of crystallographic texture, J. Mech. Phys. Solids **49**, 709-737 (2001).
[13] J. M. McNaney, V. Imbeni et al., An experimental study of the superelastic effect in a shape-memory Nitinol alloy under biaxial loading, Mech. Mater. **35**, 969-986 (2003).
[14] M. Tokuda, M. Ye et al., Calculation of mechanical behaviors of shape memory alloy under multi-axial loading conditions, Int. J. Mech. Sci. **40**, 227 - 235 (1998).
[15] E. Patoor, D. C. Lagoudas et al., Shape memory alloys, Part I: General properties and modeling of single crystals, Mech. Mater. **38**, 391-429 (2006).
[16] J. Ericksen, Symmetry and stability of thermoelastic solids, J. Appl. Mech. **45**, 740-744 (1978).
[17] J. Ericksen, Symmetry of deformable crystals, Arch. Ration. Mech. An. **72**, 1-13 (1979).
[18] J. Ericksen, Some phase transitions in crystals, Arch. Ration. Mech. An. **73**, 99-124 (1980).
[19] J. Ericksen, The Cauchy and Born hypothesis for crystals, (Academic Press, New York, 1984), 1984, p. 61-78.
[20] K. Bhattacharya, Microstructure of martensite (Oxford University Press, New York, 2003).
[21] J. Bowles and J. Mackenzie, The crystallography of martensite transformations I, Acta Metall. Mater. **2**, 129-137 (1954).
[22] J. Mackenzie and J. Bowles, The crystallography of martensite transformations II, Acta Metall. Mater. **2**, 138-147 (1954).
[23] J. Ball and R. James, Fine phase mixtures as minimizers of energy, Arch. Ration. Mech. An. **100**, 13-52 (1987).
[24] X. Wang and Z. Yue, Three-dimensional thermomechanical modeling of pseudoelasticity in shape memory alloys with different elastic properties between austenite and martensite, Mat. Sci. Eng. A-Struct. **425**, 83-93 (2006).
[25] K. Gall, H. Sehitoglu et al., The role of coherent precipitates in martensitic transformations in single crystal and polycrystalline Ti-50.8at%Ni, Scripta Mater. **39**, 699-705 (1998).
[26] P. Thamburaja, Constitutive equations for martensitic reorientation and detwinning in shape-memory alloys, J. Mech. Phys. Solids **53**, 825-856 (2005).
[27] C. Müller and O. Bruhns, A thermodynamic finite-strain model for pseudoelastic shape memory alloys, Int. J. Plasticity **22**, 1658-1682 (2006).
[28] D. Christ and S. Reese, A finite element model for shape memory alloys considering thermomechanical couplings at large strains, Int. J. Solids Struct. **46**, 3694-3709 (2009).
[29] L. Anand and M. Kothari, A computational procedure for rate-independent crystal plasticity, J. Mech. Phys. Solids **44**, 525-558 (1996).
[30] K. Gall and H. Sehitoglu, The role of texture in tension-compression asymmetry in polycrystalline NiTi, Int. J. Plasticity **15**, 69-92 (1999).
[31] A. Musienko, A. Tatschl et al., Three-dimensional finite element simulation of a polycrystalline copper specimen, Acta Mater. **55**, 4121-4136 (2007).
[32] S. Weyer, A. Fröhlich et al., Automatic finite element meshing of planar Voronoi tessellations, Eng. Fract. Mech. **69**, 945-958 (2002).
[33] A. S. J. Suiker and S. Turteltaub, Computational modelling of plasticity induced by martensitic phase transformations, Int. J. Numer. Meth. Eng. **63**, 1655-1693 (2005).
[34] T. Mura, Micromechanics of defects in solids, second edition (Martinus Nijhoff Publishers, Dordrecht, 1987).
[35] J. Lemaitre and J. L. Chaboche, Mechanics of Solid Materials (Cambridge University Press, Cambridge, 1990).
[36] G. Holzapfel, Nonlinear Solid Mechanics (John Wiley & Sons, Chichester, 2000).
[37] Z. Bo and D. C. Lagoudas, Thermomechanical modeling of polycrystalline SMAs under cyclic loading, Part I: theoretical derivations, Int. J. Eng. Sci. **37**, 1089-1140 (1999).
[38] K. Otsuka and C. M. Wayman, Shape memory materials (Cambridge University Press, Cambridge, 1998).
[39] E. W. Weisstein, Euler Angles, From MathWorld–A Wolfram Web Resource http://mathworld.wolfram.com/EulerAngles.html .
[40] J. C. Simo and T. J. R. Hughes, Computational inelasticity (Springer, New York, 1998).

[41] Y. Liu and H. Xiang, Apparent modulus of elasticity of near-equiatomic NiTi, J. Alloy. Compd. **270**, 154-159 (1998).
[42] S. Miyazaki and A. Ishida, Martensitic transformation and shape memory behavior in sputter-deposited TiNi-base thin films, Mat. Sci. Eng. A-Struct. **273-275**, 106-133 (1999).
[43] C. Niclaeys, T. B. Zineb et al., Determination of the interaction energy in the martensitic state, Int. J. Plasticity **18**, 1619-1647 (2002).
[44] I. M. Smith and D. V. Griffiths, Programming the finite element method, second edition (John Wiley & Sons, Chichester, 1988).